



Adaptive lens for foveal vision, imaging, and projection over large clear apertures

LOUIS BÉGEL,¹ BEHZAD KHODADAD,² AND TIGRAN GALSTIAN^{1,2,*}

¹Center for Optics, Photonics and Laser, Department of Physics, Engineering Physics and Optics, Université Laval, 2375 Rue de la Terrasse, Quebec, G1V 0A6, Canada

²LensVector Canada, 2375 Rue de la Terrasse, Quebec, G1V 0A6, Canada

*tigran.galstian@phy.ulaval.ca

Abstract: We report an electrically tunable liquid crystal device that enables the generation of lenses the diameters of which may be dynamically changed from sub-millimeter to multiple millimeter sizes. These lenses can be created in different regions of interest over very large (above 50 mm) optical clear apertures. The approach is based on the activation of periodically spaced contacts on a single serpentine-shaped electrode with phase-shifted electrical signals. It enables a highly reconfigurable operation of locally created lenses with variable position, diameter, optical power (OP) and aberrations. The preliminary demonstration of the capabilities of the proposed device is presented here by creating a local lens, moving its center over an area of 25 mm x 25 mm, gradually changing its diameter from 1.3 mm to 4.55 mm as well as by tuning its OP value from zero up to, respectively, ≈ 40 and ≈ 3.5 diopters. Typical driving signals are at the order of 3.5 V. We think that such lenses can be used for ophthalmic or augmented reality applications as well as in microscopy, adaptive panoramic cameras with large distorted field of view, dynamic projection, etc.

© 2023 Optica Publishing Group under the terms of the [Optica Open Access Publishing Agreement](#)

1. Introduction

During the last few decades, the tendency of optical systems for miniaturization [1] has encouraged the development of electrically variable adaptive components (for example, lenses, [2]) to enhance the performance of these systems. In the large majority of cases, it is highly desirable to achieve such adaptive capabilities without mechanical movements. Among others, mobile applications are growing significantly, and they are extremely sensitive to vibrations, shock and drop. For example, it is not convenient to use mechanical solutions for adaptive vision or even for Augmented/Virtual reality (while some of these systems still are using it because they do not have alternative solutions). In addition, size, weight, and energy consumption must be limited in such applications. Here is where the liquid crystal (LC) based solutions are very promising since rather important refractive index modulations can be achieved by locally reorienting the optical axis of the LC (the average orientation of molecular axes, called *director*, [3,4]) thanks to the dielectric torque. In addition, these components are operating with very low power consumption that is important for mobile applications. Not surprisingly, electrically tunable LC lenses (TLCLs) were intensively explored (see, for example, [5]) in various areas such as autofocus [6], wavefront modulation [7–9], depth measurement from focus/defocus [10,11], depth of field extension [12,13], etc.

Currently, there is an increased interest for devices with large clear apertures (CAs), ranging from 20 mm to 50 mm, which is first of all related to augmented reality and ophthalmic applications (for dynamic distance accommodation). Unfortunately, TLCLs with large diameters are difficult to make, particularly if we prefer refractive type lenses (see hereafter). The reason is the relatively small optical path difference $OPD = \Delta n \times L$ that can be achieved in LCs, where $\Delta n = n_{\parallel} - n_{\perp}$ is the optical birefringence (n_{\parallel} and n_{\perp} are the extraordinary and ordinary refractive indices, respectively) and L is the thickness of the LC layer. For example, if we consider a single aperture TLCL, based on the gradient index (GRIN) principle, then the achievable optical power

(OP) may be estimated as $OP = 8 \times OPD/CA^2$ [6]. Obviously, increasing the CA, for example, from 2 mm to 50 mm, decreases the achievable OP values by a factor of 625. The possibility of building such lenses by using the refractive Fresnel approach (to increase the achievable OP range) is presently being actively investigated by several groups (see, e.g., [14–17]).

However, it is important to mention that in most above-mentioned (e.g., vision/ophthalmic) applications the "detection" is performed by the human eye. It is well known that human vision can be split into foveal and peripheral vision. The foveal one, in turn, can be split between central ($\pm 2.5^\circ$), paracentral ($\pm 4^\circ$) and macular ($\pm 9^\circ$) [18]. In the case of wearing glasses, the typical distance of glass from the eye is between 12 mm and 17 mm. Thus, a tunable lens, positioned on the eye glass for foveal vision, should require a maximum diameter of 5.5 mm to be activated at each time. When the eye ball is reoriented to put another object into its foveal vision zone, then the 5.5 mm diameter zone must be activated elsewhere, on the surface of typically 50 mm total CA (largest size of eye glasses). Some change of the diameter and the profile of that lens may also be necessary.

Thus, we could work with very large optical surfaces if we could generate "local" lenses (of diameter 5.5 mm, or so) at various areas of that surface and tune their local diameters and OP values. Such an operation might be imagined by using standard LC displays (LCDs) or spatial light modulators (SLMs). However the OPD, achievable with these devices, is usually very small, e.g., $OPD = 0.5 \mu m$. Thus, only the diffractive Fresnel type solutions may be considered here with well-known difficulties related to their dichroic aberrations, focus discretization and manufacturing complexity [19]. In addition, to cover 50 mm diameters, it would require a huge number of electrodes to be controlled dynamically.

We have recently suggested (in a patent application without detailed analyzes, [17], and then with a basic study in an article [20]) a possible method of generation of relatively smooth transversal distributions of electrical potential (needed for the creation of above-mentioned refractive lenses), while using very limited number of control electrodes. It is based on a micro structured electrode layer providing very specific effective sheet resistance values, similar to those used in so-called modal control lenses. The modal control concept was pioneered by Kahn for tunable apertures [21]. Naumov's group has developed the first LC lens with the modal control approach [22]. Such a lens can be modeled as spatially distributed RC circuit and its structure is a set of layers in the following order: a low resistivity layer as a ground contact (such as indium tin oxide or ITO), an LC layer (dielectric), a high resistivity or weakly conductive layer (WCL) that improves the voltage and refractive index distribution, and a hole patterned electrode. The value of the optimal sheet resistance of the WCL is mostly defined by the lens radius and the LC thickness (Mega Ohms for mm sized diameters). On the basis of modal control LC lens, Kirby et al. have proposed a "Quad-pol" LC lens [23] that is driven by phase-shifted signals producing symmetrical electric field distribution. Kotova et al. have done research on the Quad-pol LC focusing device that implements phase delay profile in the form of a circular and elliptical cone and controls the position of the centre [24,25]. With this approach, Algorri et al. have generated microaxicon arrays [26–29]. The mentioned-above Quad-pol devices have a similar structure, and, while their electric field distributions are less affected by the change of the resistance of the WCL in the approximation of a small modal parameter, [30], the reproducible fabrication of environmentally reliable WCL remains a challenge. In addition, the radius of the lens is still limited (<10 mm) due to the use of GRIN approach. Thus, its use in relatively large aperture optical systems (ophthalmology, panoramic camera, etc.) is very limited. To avoid this limitation, refractive LC Fresnel lenses have been developed (see, e.g., [15,31]). One of these approaches ([15]) does not use WCL which is very interesting. Unfortunately, its manufacturing seems to be complicated.

In the present study, we describe an interesting development of our new WCL-free approach ([17,20]) based on the Quad-pol principle. We show that by the appropriate choice of electrode

geometry and driving method, we can create a cost effective, local, scalable, movable and tunable lens. To the best of our knowledge, such a device was not reported yet in the scientific literature. The proposed TLCL is using a matrix of control electrodes (further called, MTLCL) allowing its activation in the zone of interest at various (almost arbitrary) positions over a large optical surface. This is achieved thanks to the specific micro structured ITO pattern that is used to control the voltage distribution across the surface of the lens with a minimum number of control electrodes and without the use of WCLs, see, e.g., in [16,20,32] (see other approaches to replace the WCL in [33,34]).

2. Structure of the lens and its operation principle

The proposed device is a sandwich-like structure composed of two ITO coated glass substrates that are separated by a gap thanks to spacers of $40\ \mu\text{m}$ diameter ($L=40\ \mu\text{m}$). It can be considered as a juxtaposition of multiple smallest controllable "unit cells", reported in [20]. Figure 1(a)) schematically shows the 3D view of the structure. The ITO layers are cast at inner surfaces of these substrates and are lithographically patterned into serpentine shaped continuous electrodes (one at each substrate). Two substrates are arranged so that their serpentine electrodes have orthogonal orientations. A top view of two serpentine electrodes is shown in Fig. 1(b)). There are multiple spatially periodic electrical contacts (see, e.g., E1, E2 etc., on the top substrate and E5, E6, etc., on the bottom substrate, Fig. 1(a))), that are connected to different segments of the same serpentine electrode. This allows actively changing the electrical potential distribution in these areas. The electrical potential between these contact areas is shaped thanks to the spatial attenuation as well as the specific driving method (see hereafter). In this specific implementation, the ITO serpentine was patterned with a width w and gap g of $w=35\ \mu\text{m}$ and $g=5\ \mu\text{m}$, respectively. Commercial polyimide (PI-150) layer was cast by spin coating over the ITO pattern of each substrate, baked and rubbed in "anti parallel" directions in order to obtain a homogeneous molecular alignment. The unit cell of the device here is a square area ($0.65\ \text{mm} \times 0.65\ \text{mm}$), the top view of which is shown in Fig. 1(b)). While in principle, the number of control electrodes is not limited, in the current implementation, each substrate has 40 control contacts, resulting in a total controllable (active) area of $25\ \text{mm} \times 25\ \text{mm}$.

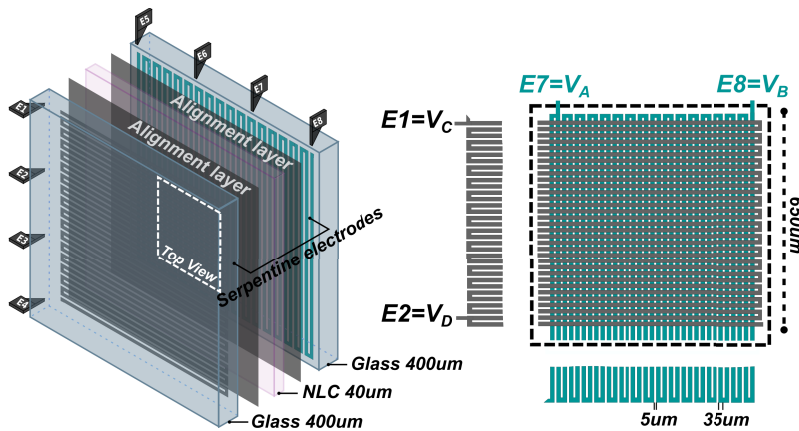


Fig. 1. Schematic demonstration of the device, a) 3D representation showing the electrode configuration and key layers, b) Top view of two cross-oriented serpentine patterns of ITO in the unit area of $0.65\ \text{mm} \times 0.65\ \text{mm}$.

The cavity (formed by two substrates) is filled with a home-made nematic LC (NLC) mixture selected because of the relatively high birefringence of $\Delta n = 0.217$.

We can start the analyzes of the operation principle of our device on the example of its unit cell [20], while the operation with larger diameters (including multiple unit cells) will be very similar, but will require the activation of control electrodes that are further from each other, like "peripheral" electrodes (V_A , V_B , V_C , and V_D , see Fig. 1(b))). In this case, intermediate control electrodes (between peripheral ones) must be managed in a well defined manner (e.g., left floating, see hereafter).

The main operation mechanism of the proposed device is based on the specific electrical resistance between control electrodes (low in comparison with the NLC's impedance) and on the combination of different phase shifts of electrical potentials applied to different control electrodes of the cell. For material and geometrical conditions that we are going to use here, this resistance generates an almost linear voltage distribution from one control electrode to another (on the same substrate) [24]. When the potentials, applied to control electrodes V_A and V_B , have a mutual phase shift of 180° (e.g., $\phi_A : 0^\circ$ and $\phi_B : 180^\circ$), then the potential at the center of this area is zero. The resulting voltage distribution on the substrate has the shape of a ramp, from $+V_A$ to $-V_B$. The same driving principle is used for electrode fingers V_C and V_D on the opposite substrate. However, in addition, these two driving signals have a common phase shift of 90° with respect to signals applied to two other electrodes (that is, $\phi_C : 90^\circ$ and $\phi_D : 270^\circ$).

The space-time distribution of the voltage U on each substrate can be described by a second-order partial differential equation taking into account the distributed RC circuit composed of the resistive serpentine ITO electrode lines (between peripheral electrodes) combined with the capacitive dielectric NLC layer between two substrates, [24,26].

$$\vec{\nabla}_s^2 U = R_s \cdot c \frac{\partial U}{\partial t} + R_s \cdot g \cdot U \quad (1)$$

where, $c = \epsilon/L$ and $g = \sigma/L$, with ϵ being the dielectric permittivity and σ the conductivity of the NLC layer. If we consider \sin driving functions (e.g., $\sin(\omega t + \phi)$) with $\omega = 2\pi f$, then the Fourier transform of the Eq. (1) allows determining the complex amplitude of the voltage U .

$$\begin{cases} \vec{\nabla}_s^2 U = \chi^2 U \\ \chi^2 = R_s(g - i\omega c) \end{cases} \quad (2)$$

We can see, from Eq. (2), that the voltage distribution is governed by the parameter χ measured in reciprocal centimetres. We can therefore expect that the distributions $U(x, y)$ will differ considerably for large and small values of χl (where l is the characteristic size of the aperture). We shall define the impedance of the structure as $Z = (g - i\omega c)^{-1}$ and the ratio between the effective sheet resistance of the serpentine electrode R_s and the impedance, as $(\chi l)^2 = R_s l^2/Z$. To be able to control the propagation of the electrical potential in the transverse plane (for different local diameters, see hereafter), the value of the resistance R_s must satisfy the condition $|\chi l| \ll 1$. In this case, the influence of the frequency on the voltage distribution becomes negligible, and the voltage distribution is controlled by the amplitude and the phase of the potential applied on control electrodes (E1, E2, etc.). The RC circuit has enough time to recharge and the potential at the centre follows the potentials' changes occurring at the peripheries, inducing a linear voltage distribution. However, we must keep R_s sufficiently high to limit the power dissipation.

This Quad-Pol lens is based on two resistive surfaces and potentials on top (U_t) and bottom (U_b) substrates. By considering $\chi_t = \chi_b = \chi$, we obtain the following voltage distributions :

$$\begin{cases} \vec{\nabla}_s^2 U_t = \chi_t^2 \cdot U_t - \chi_t^2 \cdot U_b = \chi^2 \cdot (U_t - U_b) \\ \vec{\nabla}_s^2 U_b = \chi_b^2 \cdot U_b - \chi_b^2 \cdot U_t = \chi^2 \cdot (U_b - U_t) \end{cases} \quad (3)$$

These equations may be solved, e.g., by using the finite element method on *Comsol* (in our case). For simplicity, we have considered our serpentine patterns as uniform resistive layers

(identical on both substrates) with the sheet resistance of $5 \times 10^6 \Omega/\square$, while the conductivity of the NLC was set at $\sigma \approx 10^{-9} S.m^{-1}$.

Molecules of an NLC with positive dielectric anisotropy (delta epsilon more than zero, at driving frequencies) tend to align parallel to the electrical field, and this interaction is governed by the root mean square (RMS) value of the applied voltage, $U_t - U_b$. To further simplify the analyses, we can consider the case when we use similar voltages $V_A/V_B/V_C/V_D = V$ with the same, relatively high (120 Hz), frequency F_1 . As it can be imagined from Fig. 2 (thanks to Lines 1-4), the result of the imposed relative phase shift is a continuous change (with rotation) of the electric field and the creation of an RMS voltage distribution of conical shape (see its cross section in Fig. 3(a))). In the described geometry, NLC molecules can be reoriented only if the applied voltage exceeds a certain threshold value V_{th} [3,4]. Thus, due to the above-described electric potential distribution profile and the existence of that threshold, there will be an area in the center of the cell where molecules will not be reoriented and the phase delay (of light traversing this area) will remain constant. This plateau can be eliminated in several ways, e.g., by adjusting the phase between two parallel electrodes on the same substrate (e.g., 160° instead of 180°) or by adding a low frequency offset V_{off} (see curved dashed lines in Fig. 2) to two electrodes of the same substrate or by adding specific phase-shifted offset signals to all electrodes [23,28,35], (see Fig. 3(b))). The alternative offset component of the driving signal is shifting the instantaneous position of the zero volts in the transverse plane (between positions $-z_0$ and $+z_0$, see Fig. 3(b)). It helps to shift-up the RMS voltage profile such that there is no region under the threshold voltage ($V_{off} \geq V_{th}$) of LC (see Fig. 3(b)) as well as to increase the curvature of the potential in the center of the lens.

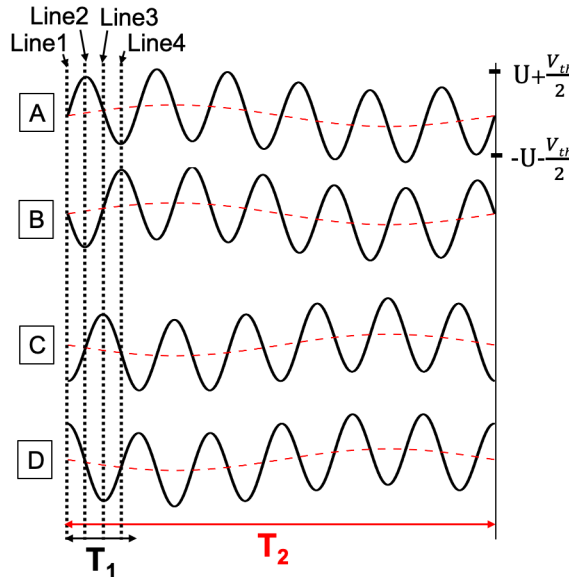


Fig. 2. Schematic demonstration of 4 phase-shifted electrical control signals (applied to contacts A, B, C and D) with an additional low frequency offset voltage shown by 4 horizontal curved dashed lines, with periods $T_1 = 1/F$ and $T_2 = 1/f$, respectively. Vertical dashed lines 1-4 show the phase shift between signals: Line 1 correspond to phase 0, Line 2 : $\pi/4$, Line 3 : $\pi/2$ and Line 4 : $3\pi/2$ of the period T_1 .

In order to generate the above-mentioned 4 electrical signals, a driving module has been designed and built. It consists of a custom electrical phase shift waveform generator. The micro controller (coupled with buffers/inverters) can generate two 90° phase-shifted electrical signals

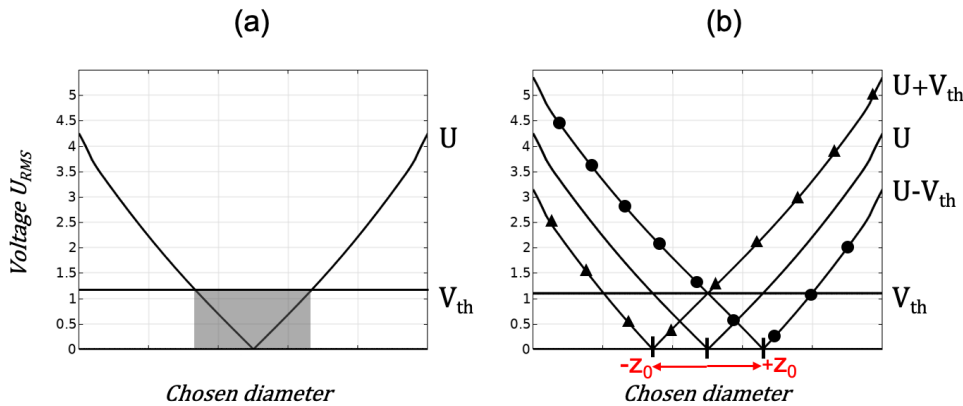


Fig. 3. Cross sectional view of V_{RMS} voltage distribution along X and Y axis, over the oscillation cycle; a) No offset voltage is applied; the dark rectangle corresponds to the area of the lens below threshold voltage, b) Adding alternative offset equal to V_{th} : during the first half period T_2 of the offset (filled triangles correspond to the top substrate voltage distribution profile and filled circles correspond to the bottom substrate), and vice versa for the second half period (see main text for details).

with high-frequencies F_1 and F_2 (in our implementation, $F_1=F_2=F$), as well as one signal with low-frequency f . These signals are combined as shown Fig. 2(a) to produce 4 signals on contacts A, B, C and D. Finally, multiplexers are used to generate the drive outputs. These multiplexers can select open-circuit (floating), one of the A/B/C/D signals, or ground to be applied to electrodes.

3. Experimental results

We have started the experimental characterization of our device by observing traditional interference fringes captured by placing the lens between two crossed polarizers with the rubbing direction of the NLC oriented at 45° from the linear polarization at the input as shown Fig. 4(a) [36].

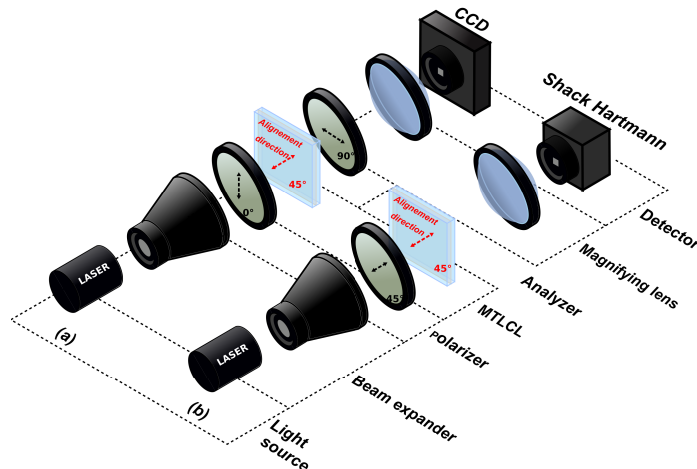


Fig. 4. Schematic presentations of experimental setups used for lens characterization. (a) polarimetric measurements, (b) Shack-Hartmann wavefront sensing.

In this case, both extraordinary and ordinary polarized propagation modes will be generated inside the NLC layer. They will exit from the cell with different phase delays at different transversal positions (when the lens is activated), and will interfere thanks to the second polarizer (analyzer) oriented at 45° with respect to the ground state molecular orientation of the NLC. Thus, two neighboring constructive (bright line) or destructive (dark line) interference fringes represent an optical phase difference of 2π . The obtained OPD can be easily converted into phase delay by multiplying it by $2\pi/\lambda$. One can see examples of such interference fringes in Fig. 5(a)) for three different values of the OP of the same lens (same diameter). This can give us a first visual information concerning the obtained wavefront profiles. We can use them also for a quantitative analyses. However, we can obtain more precise quantitative data by using a Shack-Hartmann wavefront sensor (described in Fig. 4(b)). For example, Fig. 5(b) and Fig. 5(c) demonstrate such wavefronts for excitation voltage values ranging from $1.5 V_{RMS}$ to $5.5 V_{RMS}$ (see the right vertical axis). The frequency of main excitation signals here was $F=120$ Hz during all this experiment and the frequency of the offset signal was $f=20$ Hz.

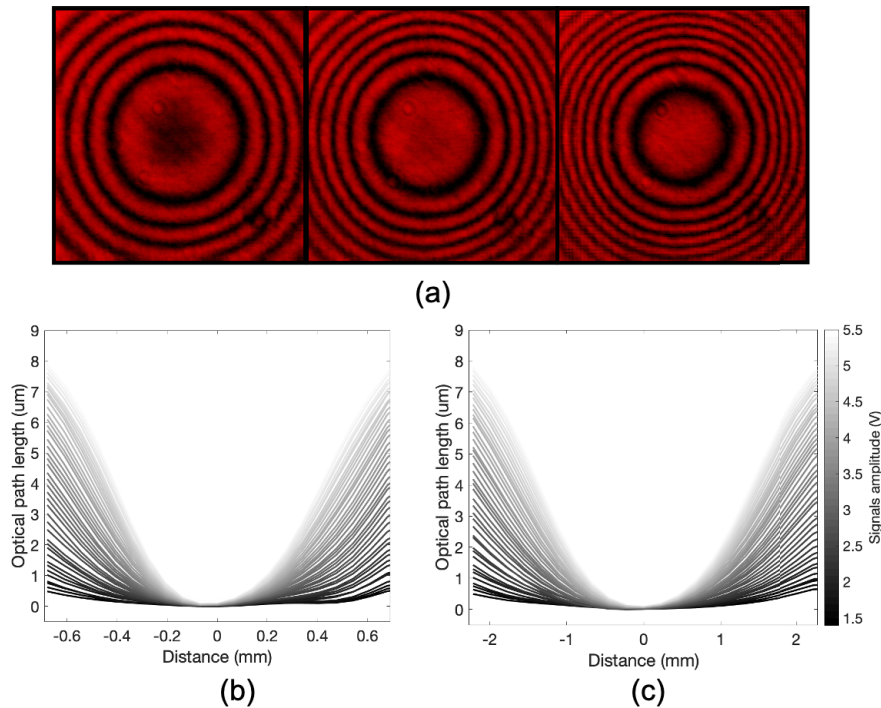


Fig. 5. a) Polarimetric interference patterns for $V = 2 V_{RMS}$, $2.5 V_{RMS}$ and $3.0 V_{RMS}$, from left to right, respectively, and $V_{off} = 1.2 V_{RMS}$, (b and c) Optical path length for two different lens diameters (1.3 mm and 4.55 mm), obtained from Shack Hartmann measurements, with increment of $0.1 V_{RMS}$.

Figure 5 shows the capability of this lens to progressively increase its OP by increasing the voltage value applied on control electrodes (see hereafter for quantitative measurements of corresponding aberrations). This demonstration was performed qualitatively for a given diameter (Fig. 5(a)) and, in a more detailed way, for two specific diameters, 1.3 mm and 4.55 mm, Fig. 5(b) and Fig. 5(c), respectively. However, as we have already mentioned, the proposed design has the capability of gradually scaling the size of the lens diameter. If we wish to increase the CA, then we must keep in mind that our lens is a GRIN lens, and thus its OP decreases quadratically with

the aperture size of the local lens. Also, to generate local lenses with larger CA, we must choose a different sheet resistance for the ITO to keep aberrations low.

To demonstrate this capability, the control contacts A, B, C and D were first selected as peripheral electrodes (defining the desired size of the lens), and excitation signals were applied to them. All inner electrodes (between the peripheral ones) were left in the floating (F) states. The low resistance serpentine electrode pattern, we have designed here for a specific application, allows to easily generate from simple ($\phi=0.65$ mm) up to septuple lens sizes ($\phi =4.55$ mm), see Fig. 6, with the same character of voltage distribution. The top left picture in Fig. 6 shows the interference pattern of the device in the ground state. The large curved dark zone between two bright zones is witnessing the slightly non uniform gap (thickness) of the NLC due to the fabrication imperfections. The picture at the top right demonstrates the generation of a small diameter lens (CA=0.65 mm). The following pictures (below) show larger lenses, obtained by pushing peripheral electrodes farther from each other. The last picture (bottom right) shows the example of a lens with CA=4.55 mm.

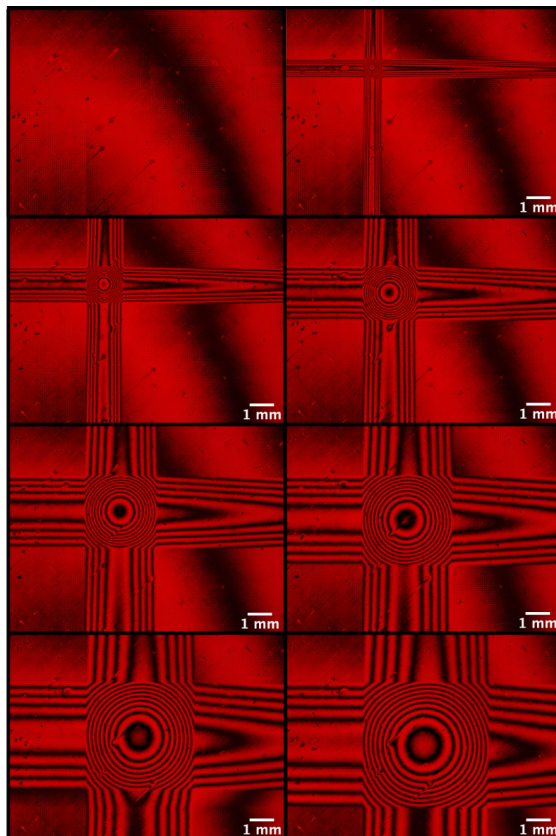


Fig. 6. Interference pattern for several lens sizes, ranging from CA = 0.65 mm to CA = 4.55 mm, V = 3.2 V_{RMS} and V_{off} = 1.2 V_{RMS}.

Corresponding wavefronts were quantitatively characterized by using a probe beam of extraordinary polarization mode (the incident beam was linearly polarized along the rubbing direction of the polyimide). Our experimental procedure was as follows (see Fig. 4(b)) [32]). The reference wavefront was recorded without the MTLCL by using a Shack-Hartmann wavefront sensor (Thorlabs). Then, we have introduced the MTLCL and aligned its position (x,y, and z) by using micrometric tables. A relay lens was used to image the output plane of the MTLCL on

the sensor plane of the Shack-Hartmann sensor. For a given voltage and frequency of excitation signals, aberrations of the lens were measured and analyzed using Zernike coefficients. We have measured up to the 66th Zernike polynomials, but we shall discuss only aberrations between the orders 0 to 4; according to Zernike classification, these first-order aberrations are responsible for main deformations of the wavefront [18]. Zernike polynomials are orthogonal over a unit circle and represent optical aberrations over a circular pupil. These characteristics are lost when non circular pupils are employed. Some schemes for square pupils have obtained square polynomials [37] from the orthogonalization of circle polynomials [38], using a circle inside the square. This procedure has the disadvantage of losing the part of the wavefront that falls outside the circle. Some other studies overcome this problem by defining a unit square inside the circle [39]. However, these orthogonalizations are theoretical interpretations of square wavefront shape from circular shape, so we shall not investigate this question here since our main goal is to show the main capabilities (here, the tunability) and size variations for circular apertures only.

As it is shown in Fig. 7, the obtained OPs (in diopters) are indeed inversely proportional to the square of the lens size, as predicted. We experimentally reach 40 diopters of OP for the double lens ($\varnothing=1.3$ mm) in comparison with the septuple lens ($\varnothing=4.55$ mm) the maximum OP of which is reaching 3.5 diopters. For constant frequency and amplitude values, the wavefront is theoretically identical for each lens size due to linear voltage distribution. Indeed, the total RMS aberrations show the same tendency for all diameters. Up to $V = 3.6 V_{RMS}$, the total RMS error is below $0.2 \mu\text{m}$. Spherical RMS aberrations are representing the majority of the wavefront deformations in these lenses. Up to $3.5 V_{RMS}$, the generated lens maintains a good spherical profile, but for higher voltage values, spherical aberrations increase, and the lens' shape tends to a conical profile (generating an axicon).

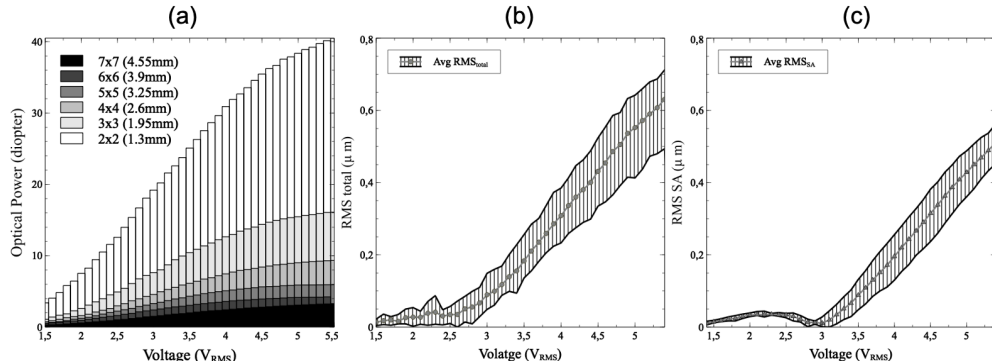


Fig. 7. Optical characterization of lenses of various sizes, ranging from 1.3 mm to 4.55 mm, a) OP vs voltage, b) Total RMS wavefront error vs voltage, c) RMS wavefront error for spherical aberrations vs voltage. Hatched zones correspond to max and min values measured for each lens size.

In the next section, we demonstrate the capability of the proposed design to change the position of the local lens. Indeed, when the desired position (the center) of the lens and its diameter are decided, then we activate the peripheral control electrodes (A, B, C and D) that are centered around the desired position and spaced (separated) from each other to provide also the desired diameter. All the rest of the procedure is the same. To move the center of the lens, the same four signals are applied on different peripheral electrodes that are centered now around the new position. Obviously, if we desire to keep the same diameter, then the distance between these peripheral electrodes must be kept constant, see the corresponding example in Fig. 8. To facilitate the discussion of these localized lenses, vertical and horizontal references (by numbers and letters,

respectively) were added to easily identify their positions. In this particular demonstration, the diameter was kept constant (1.3 mm).

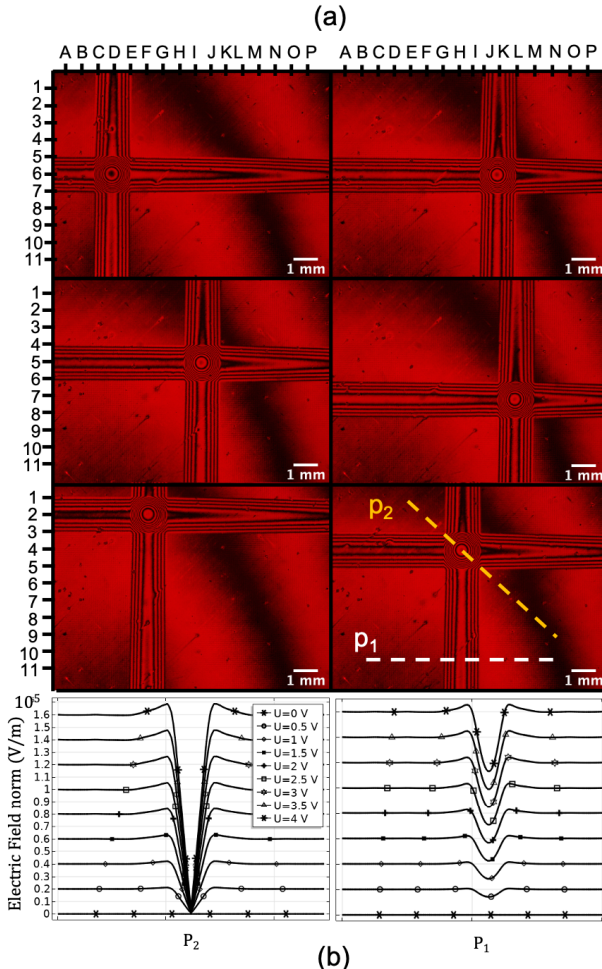


Fig. 8. a) Interference patterns for several positions of a lens (with the same CA = 1.3 mm) through the surface of the MTLCL. $V = 3.2 V_{RMS}$ and $V_{off} = 1.2 V_{RMS}$; b) Electric field's profile through the active lens (line P_2) and through the addressing electrodes (line P_1).

It is also interesting to analyze (see Fig. 8) the wavefront scans across the lens (by diagonal, along the dashed line P_2) as well as across the "traces" generated by the activation of control electrodes (along the dashed line P_1). It is clear that, in this implementation, we have generated a good lens (see bottom left, Fig. 8(b)) in the central zone of interest, while there is also a relatively weak cylindrical lens created between the peripheral electrodes (see bottom right, Fig. 8(b)). Here also, we can use the spatial frequency of interferential fingers to evaluate the corresponding profile changes.

If desired, we can reduce the cylindrical lensing effect in regions outside the active lens. This may be done by avoiding (or reducing) the abrupt drop (or change) of the electric potential and corresponding molecular reorientations in these areas. For example, if the electric potential, applied on external (around the zone of interest) electrodes, are close to V_{sat} (with V_{sat} being the reorientation saturation voltage) then all the NLC, around the active lens, will be completely reoriented (tending to homeotropic alignment), and the active lens will then be better localised.

In our case, due to the driver limitation, we were able to apply on external electrodes (out of the zone of interest) only a voltage V similar to those applied on electrodes A, B, C and D, see Fig. 9(d). However, we are convinced that the application of higher voltages $V_{ext} > V$ can induce a fully localised lens. In the opposite case, our simulations and measurements confirm that, if the outer electrodes were left floating (Fig. 9(b)) or grounded (Fig. 9(c)), then the voltage drop increased. When the same signals were applied also to external electrodes, it induced a relatively uniform electrical potential in the outer area (Fig. 9(d)).

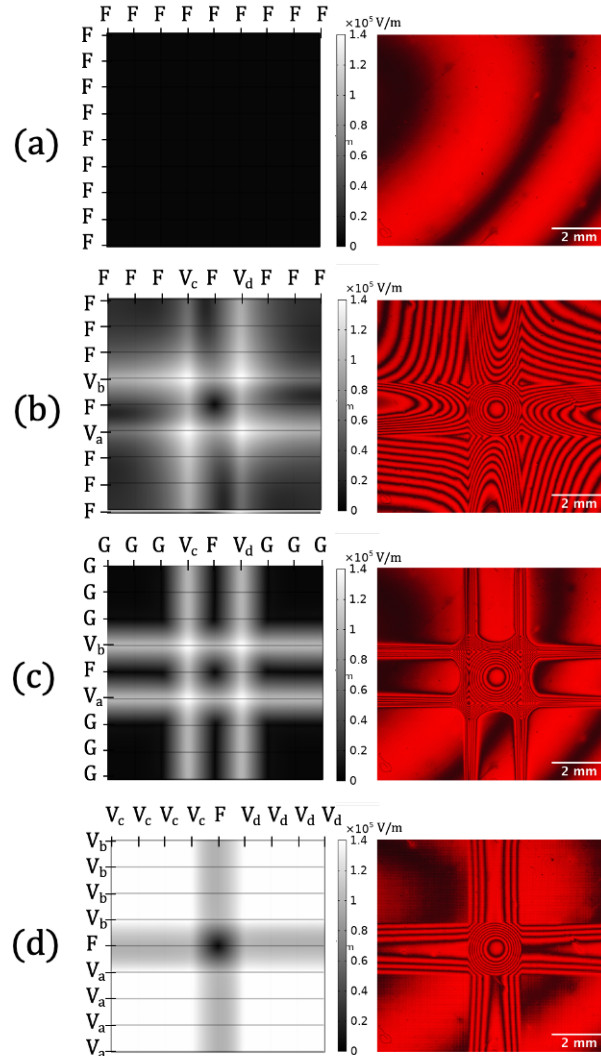


Fig. 9. Left column: theoretical simulations of the electric field distribution depending upon the external electrodes' states, floating : F; ground : G; V_a, V_b, V_c and V_d : A/B/C/D signals. Right column: experimental observations of the interference pattern. a) Reference image, all electrodes are in the floating (off) state. Lens generation : b) applied 4 phase shifted signals $V_a/V_b/V_c$ and V_d , while maintaining external electrodes in floating states. c) external electrodes are in Ground state. d) external electrodes are in the same state as the control signals applied to the peripheral control electrodes of the desired zone.

Furthermore, to evaluate the local improvement of image quality, the MTLCL was positioned in front of a standard commercial camera (Raspberry Pi Module v2 combined with 6 mm wide angle lens). The camera lens was adjusted to have target objects (books) out of focus. Then, a local lens of diameter 3.9 mm was activated and its OP was adjusted to bring one part of the scene (the note "Think Python" positioned at approximately 37 cm) in focus. The corresponding voltage was $3.6 V_{RMS}$ and the OP was 4D. Figure 10 shows the difference between the out of focus image (with the MTLCL disabled but still in front of the camera, Fig. 10(a)) compared to the case when the MTLCL was activated Fig. 10(b). The corresponding improvement of the modulation transfer function of the system is demonstrated in Fig. 10(c), there is no copy right issues; we have recorded this image by using commercially available books.

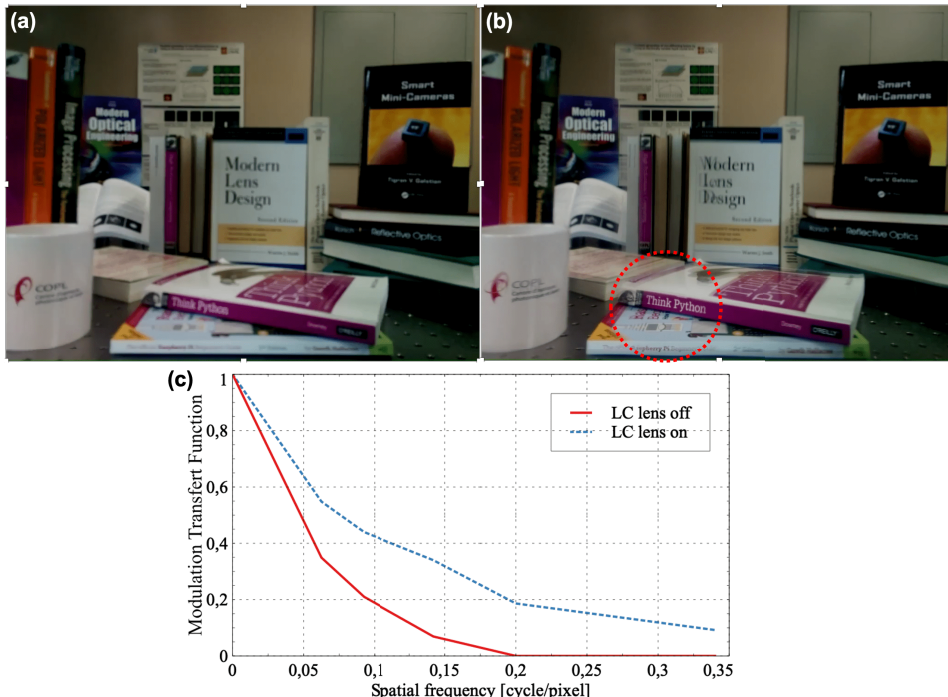


Fig. 10. Impact of the MTLCL on the local image quality recorded on a random scene by using a commercial Raspberry Pi camera combined with MTLCL, a) original photo, MTLCL is off. b) photo with a local lens (with 3.9 mm diameter) activated (at $3.6 V_{RMS}$), focused on the area "Think Python". c) the corresponding modulation transfer functions of the region of interest.

4. Discussions and conclusions

The capability of creating tunable lenses in different positions and changing their diameters seems to be a very interesting feature when dealing with large optical surfaces where the standard GRIN approach is not efficient over the entire surface, but the zone of interest may be dynamically localized. The proposed design could be very promising first of all to enhance the vision (ophthalmic, augmented reality, etc.) and imaging (microscopy, endoscopy, panoramic cameras with distorted large field of view, etc.). Its applications in various display and projection systems also is quite possible. In many of above-mentioned applications there are indeed local zones of interest changing dynamically. Obviously, these applications have various requirements in terms of performances. The variability range of the OP and corresponding aberrations of

obtained here lenses are similar to traditional modal lenses and should be acceptable for the majority of these applications.

In the presented here implementation, we observe wavefront perturbation outside the zone of interest, but in many above-mentioned applications that zone has less importance. Human tests we have started recently confirm this hypothesis (a corresponding manuscript is in preparation). However, as we have mentioned above, if desired, it will be possible also to create fully localised lenses, without noticeably disturbing the external area, by modifying the driver.

Concerning the zone of interest for foveal vision : we have already mentioned that 5.5 mm diameter lenses might be large enough to insure a clear foveal vision. Our current demonstration was made with lenses of CA=4.55 mm (designed for a different application), which were providing 3.5 diopters of OP. If we use the inverse square rule of tunable GRIN lenses, we should be able to generate 2.4 diopters of OP for 5.5 mm diameter lenses. According to our discussions with ophthalmology experts, this should cover the large majority of customers. In addition, thanks to the specific electrode structure of the local lens and its driving technique, we have much richer wavefront control capabilities. Namely, we can generate also cylindrical lenses, axicons, etc. (e.g., for compensating astigmatism, coma, etc.).

For the current implementation, we have used 0.65 mm as the minimum distance between control electrodes, which defines the minimum diameter (or the unit cell size) of the lens. Also, the external size of the optically active area was 25 mm x 25 mm. However, there is no fundamental reason why we could not change these values. From the point of view of the local lens; the main limiting factors, to obtain smaller sizes, shall be related to the choice of the ITO's sheet resistance R_s and to the thickness of substrates used. Indeed, in some cases (not always) a polarization independent operation will be required. Thus, we would need to laminate two such devices together (cross oriented, see, e.g., [6]), with NLC layers as close as possible to avoid the polarization related aberrations [40]. For larger sizes (still for the local lens), the main optimization should be related to the choice of the R_s . For such sizes, we can increase the thickness of the LC layer to partially compensate the loss of the OP, but this must be done considering also the speed and scattering requirements of target application.

In terms of the external size of the device (the active area over which we can move the local lens) - we do not see limitations, except the number of connections, which, by the way, is much smaller in our case compared to traditional LCDs and SLMs.

The fact that we create such lenses without using a WCL is another important advantage from the manufacturing (cost) point of view. Indeed, our patterned ITO is rather simple to manufacture in a single lithographic step, compared to the WCL. Finally, with very low voltages (below 5.5 V_{RMS}) and frequencies (20 - 120 Hz), required for the control, this device will feature very low power consumption that is another important advantage for mobile (e.g., ophthalmic or augmented reality) applications.

There are still important characterizations to be done, such as the speed (currently, the Activation/Relaxation times are at the order of 0.2 sec and 0.8 sec, respectively) and haze measurements and their possible optimizations (if required by the specific application), but we can already state that the proposed device has very high potential for applications.

Acknowledgments. We would like to thank LensVector for the financial and material support. We would like to express a special thank to A. Bagramyan for his help in the process of lens prototyping.

Disclosures. Authors declare no conflict of interest.

Data availability. Detailed data underlying the results, presented in this paper, are not publicly available at this time, but may be obtained from authors upon request.

References

1. T. Galstian, *Smart mini-cameras*, vol. 258 (CRC press Boca Raton, 2014).
2. S. Sato, "Liquid-crystal lens-cells with variable focal length," *Jpn. J. Appl. Phys.* **18**(9), 1679–1684 (1979).
3. P.-G. De Gennes and J. Prost, *The physics of liquid crystals*, 83 (Oxford university press, 1993).

4. V. G. Chigrinov, *Liquid crystal devices: physics and applications* (Artech House, 1999).
5. Y.-H. Lin, Y.-J. Wang, and V. Reshetnyak, "Liquid crystal lenses with tunable focal length," *Liq. Cryst. Rev.* **5**(2), 111–143 (2017).
6. T. Galstian, O. Sova, K. Asatryan, V. Presniakov, A. Zohrabyan, and M. Evensen, "Optical camera with liquid crystal autofocus lens," *Opt. Express* **25**(24), 29945–29964 (2017).
7. S. Kotova, V. Patlan, S. Samagin, and O. Zayakin, "Wavefront formation using modal liquid-crystal correctors," *Phys. Wave Phen.* **18**(2), 96–104 (2010).
8. L. Begel and T. Galstian, "Dynamic compensation of gradient index rod lens aberrations by using liquid crystals," *Appl. Opt.* **57**(26), 7618–7621 (2018).
9. L. Begel and T. Galstian, "Liquid crystal lens with corrected wavefront asymmetry," *Appl. Opt.* **57**(18), 5072–5078 (2018).
10. S. Emberger, L. Alacoque, A. Dupret, C. L.-M. de Boissac, d. l. T. de Bougrenet, J. Louis, and N. Fraval, "Liquid crystal lens characterization for integrated depth sensing and all in focus imaging application," *Electron. Imaging* **29**(6), 34–39 (2017).
11. Y. Lei, Q. Tong, X. Zhang, H. Sang, A. Ji, and C. Xie, "An electrically tunable plenoptic camera using a liquid crystal microlens array," *Rev. Sci. Instrum.* **86**(5), 053101 (2015).
12. Y.-J. Wang, X. Shen, Y.-H. Lin, and B. Javidi, "Extended depth-of-field 3d endoscopy with synthetic aperture integral imaging using an electrically tunable focal-length liquid-crystal lens," *Opt. Lett.* **40**(15), 3564–3567 (2015).
13. A. Bagramyan, T. Galstian, and A. Saghatelian, "Motion-free endoscopic system for brain imaging at variable focal depth using liquid crystal lenses," *J. Biophotonics* **10**(6–7), 762–774 (2017).
14. J. Bailey, P. B. Morgan, H. F. Gleeson, and J. C. Jones, "Switchable liquid crystal contact lenses for the correction of presbyopia," *Crystals* **8**(1), 29 (2018).
15. A. Jamali, D. Bryant, A. K. Bhowmick, and P. J. Bos, "Large area liquid crystal lenses for correction of presbyopia," *Opt. Express* **28**(23), 33982–33993 (2020).
16. Z. Zemska and T. Galstian, "Electrically tunable lens with a non-monotonic wavefront control capability," *Opt. Lett.* **47**(17), 4287–4290 (2022).
17. T. Galstian, "Electrode structure for creating electrical potential gradient, pct patent appl," Tech. rep., PCT/CA2020/051688, publ. No. WO 2021/113963 (2020).
18. W. J. Smith, *Modern optical engineering: the design of optical systems* (McGraw-Hill Education, 2008).
19. P. Valley, D. L. Mathine, M. R. Dodge, J. Schwiegerling, G. Peyman, and N. Peyghambarian, "Tunable-focus flat liquid-crystal diffractive lens," *Opt. Lett.* **35**(3), 336–338 (2010).
20. J. Stevens and T. Galstian, "Electrically tunable liquid crystal lens with a serpentine electrode design," *Opt. Lett.* **47**(4), 910–912 (2022).
21. F. Kahn, "Electronically variable iris or stop mechanisms," (1973). US Patent 3, 741, 629.
22. A. Naumov, M. Y. Loktev, I. Guralnik, and G. Vdovin, "Liquid-crystal adaptive lenses with modal control," *Opt. Lett.* **23**(13), 992–994 (1998).
23. A. K. Kirby, P. J. Hands, and G. D. Love, "Liquid crystal multi-mode lenses and axicons based on electronic phase shift control," *Opt. Express* **15**(21), 13496–13501 (2007).
24. S. P. Kotova, V. V. Patlan, and S. A. Samagin, "Tunable liquid-crystal focusing device. 1. theory," *Quantum Electron.* **41**(1), 58–64 (2011).
25. S. P. Kotova, V. Patlan, and S. A. Samagin, "Tunable liquid-crystal focusing device. 2. experiment," *Quantum Electron.* **41**(1), 65–70 (2011).
26. J. Algorri, G. Love, and V. Urruchi, "Modal liquid crystal array of optical elements," *Opt. Express* **21**(21), 24809–24818 (2013).
27. J. Algorri, V. Urruchi, N. Bennis, J. Sánchez-Pena, and J. Otón, "Tunable liquid crystal cylindrical micro-optical array for aberration compensation," *Opt. Express* **23**(11), 13899–13915 (2015).
28. J. F. Algorri, V. Urruchi, N. Bennis, P. Morawiak, J. M. Sánchez-Pena, and J. M. Otón, "Liquid crystal spherical microlens array with high fill factor and optical power," *Opt. Express* **25**(2), 605–614 (2017).
29. J. F. Algorri, V. Urruchi, B. García-Cámarra, and J. M. Sánchez-Pena, "Liquid crystal lensacons, logarithmic and linear axicons," *Materials* **7**(4), 2593–2604 (2014).
30. G. Vdovin, I. Guralnik, S. P. Kotova, M. Y. Loktev, and A. F. Naumov, "Liquid-crystal lenses with a controlled focal length. i. theory," *Quantum Electron.* **29**(3), 256–260 (1999).
31. O. Sova and T. Galstian, "Modal control refractive fresnel lens with uniform liquid crystal layer," *Opt. Commun.* **474**, 126056 (2020).
32. A. Pusenkova, O. Sova, and T. Galstian, "Electrically variable liquid crystal lens with spiral electrode," *Opt. Commun.* **508**, 127783 (2022).
33. J. Algorri, P. Morawiak, D. Zograopoulos, N. Bennis, A. Spadlo, L. Rodríguez-Cobo, L. R. Jaroszewicz, J. Sánchez-Pena, and J. M. López-Higuera, "Multifunctional light beam control device by stimuli-responsive liquid crystal micro-grating structures," *Sci. Rep.* **10**(1), 13806 (2020).
34. J. F. Algorri, P. Morawiak, D. C. Zograopoulos, N. Bennis, A. Spadlo, L. Rodriguez-Cobo, L. R. Jaroszewicz, J. M. Sanchez-Pena, and J. M. Lopez-Higuera, "Cylindrical and Powell liquid crystal lenses with positive-negative optical power," *IEEE Photonics Technol. Lett.* **32**(17), 1057–1060 (2020).

35. Y. Zhang, G. Li, X. Chen, and M. Ye, "Driving methods for liquid crystal lens with rectangular aperture and four voltages," *Jpn. J. Appl. Phys.* **60**(10), 102002 (2021).
36. L. Tabourin and T. Galstian, "Liquid crystal module for motionless generation of variable structured illumination," *J. Opt. Soc. Am. B* **37**(7), 2064–2070 (2020).
37. G.-m. Dai and V. N. Mahajan, "Orthonormal polynomials in wavefront analysis: error analysis," *Appl. Opt.* **47**(19), 3433–3445 (2008).
38. M. Bray, "Orthogonal polynomials: a set for square areas," in *Optical Fabrication, Testing, and Metrology*, vol. 5252 (International Society for Optics and Photonics, 2004), pp. 314–321.
39. V. N. Mahajan and G.-m. Dai, "Orthonormal polynomials in wavefront analysis: analytical solution," *J. Opt. Soc. Am. A* **24**(9), 2994–3016 (2007).
40. A. Bagramyan and T. Galstian, "Dynamic control of polarization mismatch and coma aberrations in rod-grin assemblies," *Opt. Express* **27**(10), 14144–14151 (2019).